

An insect larvae inspired MXene-based jumping actuator with controllable motion powered by light

Liangliang Xu^a, Fuhua Xue^a, Haowen Zheng^a, Qixiao Ji^b, Changwen Qiu^b, Zhong Chen^a, Xu Zhao^a, Pengyang Li^a, Ying Hu^{b,*}, Qingyu Peng^{a,*}, Xiaodong He^{a,*}

^a National Key Laboratory of Science and Technology on Advanced Composites in Special Environments, Center for Composite Materials and Structures, Harbin Institute of Technology, Harbin 150080, PR China

^b Institute of Industry & Equipment Technology, Hefei University of Technology, Hefei 230009, PR China

ARTICLE INFO

Keywords:

Jumping actuator
Soft robotics
MXene
Biomimetic devices
Photoactuators

ABSTRACT

Many creatures in nature can carry objects to precisely jump, however, this is difficult to achieve in untethered artificial soft robots. Here, by mimicking the latching mechanism of the insect larva jumping, an untethered MXene-based soft actuator with adjustable jumping motion controlled by light is designed. The actuator prepared by the large size MXene nanosheets and polymer has an original closed rolled structure with an adhesive coating serving as a latch, which perfectly simulates the formed loop of the insect larva before jumping. Under light, due to the storage and sudden release of light-driven elastic energy caused by the latch, the actuator produces jumping motion. More importantly, by regulating irradiation angle to locally irradiate the actuator, it can generate elastic forces in different directions, realizing different jumping motions including high jump and long jump. Moreover, the actuator's ability to carry a load for high jump under light is also demonstrated.

1. Introduction

In nature, jumping is an important locomotion way for many creatures. For example, when in danger, some worm-like insect larvae can elastically load their body into a taut loop, then jump to escape by releasing the elastic energy brought by compressing their bodies [1,2]. Jumping spiders (*Salticidae*) can catch prey or avoid natural enemies by accurate jumping motion, which is achieved by pressurizing their inner body fluid [3,4]. Insect-parasitic nematodes (*Steinernema carpocapsae*) are triggered to jump towards the hosts through using surface tension of water to adhere the head and tail to form a loop by the presence of the host-associated volatile cues, and attack them [5]. Due to the high efficiency and fast locomotion in jumping motion compared with that of the crawling motion, it is highly desirable to develop jumping motion in artificial robotic systems, which show great prospective in industrial, environment exploration, and military applications [6–8]. For example, jumping robots are expected to complete part of works that previously only achieved by aircraft, such as collecting vision-based data of the ground below; on low gravity planets, jumping robots can jump higher to facilitate tasks [9]. However, the traditional rigid robotics needs motor, spring, and delicate energy control to realize the jumping

motion, which leads to the complicated structure and the limitation in miniaturization. In contrast, in these biological systems, the elastic energy from the soft muscle can be stored, amplified and then rapidly released to powerful jumping with precise motion control, providing a new inspiration for the design of jumping robots [1,2,5,10,11]. Therefore, mimicking the so-called power-amplified biological systems in artificial soft actuation systems is crucial for developing novel soft jumping microrobots, which requires the design of artificial muscle actuator and elaborate elastic structure for energy storage and release [10,12,13].

Soft actuators, also named as artificial muscles [14], are special energy transduction smart devices that can output mechanical energy under the stimulation of external energy stimuli (e.g., light [15–22], electric [21,23–25], heat [15,26–29], and chemical molecules [19,30,31], etc.). Among them, actuators powered by light have attracted considerable attention due to the advantages including remote powering, no contact actuation, and local stimulation, which possesses great potential in developing untethered soft jumping robots and devices [32,33]. In recent years, by using various material components, actuator structure, and actuation mechanism, researchers have developed several types of untethered soft actuators and robots with jumping motion. Aida

* Corresponding authors.

E-mail addresses: huying@hfut.edu.cn (Y. Hu), pengqingyu@hit.edu.cn (Q. Peng), hexd@hit.edu.cn (X. He).

<https://doi.org/10.1016/j.nanoen.2022.107848>

Received 16 July 2022; Received in revised form 5 September 2022; Accepted 22 September 2022

Available online 24 September 2022

2211-2855/© 2022 The Authors. Published by Elsevier Ltd. This is an open access article under the CC BY-NC-ND license (<http://creativecommons.org/licenses/by-nc-nd/4.0/>).

et al. [19] fabricated a carbon nitride film actuator with anisotropic layered structure that can jump high under light irradiation due to the deformation induced by water desorption. Hu et al. [34] designed a light-driven jumping robot based on carbon nanotube/polymer bilayer actuator. By mimicking human's flicking finger motion, the soft jumping robot could jump high up to 32 mm (5 times higher than its own height) under light irradiation. Sitti et al. [35] reported a light-powered in-air hydrogel actuator composed of a binary iron oxide nanoparticle and PAANA hydrogel composite. It exhibits a superior jumping performance under light due to synergetic interactions between the elasticity of the hydrogel and the bubble caused by the photothermal effect of the embedded iron oxide nanoparticles. Very recently, Liu et al. [30] fabricated a shrimp-shell-structured poly(indenoquinacridone)/carbon nanotube sheet bilayer actuator that can jump as high as 26 mm in exposure to the CH_2Cl_2 vapor. Crosby et al. [36] also reported a jumping actuator based on PDMS and n-hexane gel. Due to the transient de-swelling of n-hexane solvent in PDMS networks, it can realize repeatable jumping locomotion. Zeng et al. [37] reported a jumping actuator based on photo-responsive liquid crystal elastomer (LCE) and photothermal liquid crystal (LC). The LCE stores energy under the irradiation of green light, and the photothermal LC produces a crystal-to-liquid transition under the irradiation of blue light to release the stored energy, which causes the actuator to produce a jump movement. Although important progress has been made in jumping robots, controllable jumping locomotion with tunable mode (high jump or long jump) and ability of carrying object is seldom realized in untethered soft robot systems due to difficulties in integration of actuator, latch, and precise energy control and release in a spatially efficient way.

In this paper, by mimicking the jumping motion of gall midge larvae involving the latch-mediated spring actuation mechanism, we design a soft jumping actuator based on large size MXene nanosheet composite film, and realize the adjustable jumping motion and load capacity powered and controlled by light. MXene ($\text{Ti}_3\text{C}_2\text{T}_x$) is a new type of two-dimensional transition metal carbides and/or nitrides with excellent optical, electrical, and thermal properties [38–40], which have been widely used in soft actuation fields [41–46]. However, up to now, the research work about the construction of jumping robot by using MXene as component is still rare. Here, we fabricate a closed rolled MXene/polymer composite film with excellent photothermal actuation and mechanical elasticity by utilizing the interfacial thermal stress in high temperature, and introduce uncured viscous polymer coating as the latch, so as to design the gall midge larva-like photoactuator. The actuator not only simulates the closed loop state of the gall midge larvae before taking off, but also further simulate its latching mechanism, which can realize the jumping motion similar to gall midge larvae. Compared with the composite film without adhesive latch, the gall midge larva-like actuator can store and then release the light-driven deformation energy through the latch, producing rapid ejected deformation from closed loop to stretched plane. The deformation process is completed in only 50 ms and the speed is as high as $6000^\circ \text{ s}^{-1}$. Based on this photoactuator, a light-driven jumping actuator is further designed. When placed on the ground, the light-driven deformation of the jumping actuator is temporarily prevented by the adhesion of latch, leading to the accumulation of the elastic energy. Once the latch opens, the transient stored elastic energy launches the actuator into the air, generating jumping motion. More importantly, by selectively irradiating the specific area of the actuator, the directions of the force applied to the ground by the actuator can be adjusted, so that the jumping motion can be precisely controlled. When the light is incident in parallel (irradiation angle of 0°), the actuator produces long jump in horizontal direction; when the irradiation angle is changed to 30° , it produces high jump in vertical direction with the height up to 41 mm (10.3 times of its own height). The regulation mechanism of the light-driven jumping motion is also discussed. Moreover, the jumping actuator can also carry an object a weight of 0.5 times its own weight to jump to 33.4 mm height, which has never been realized in the current untethered soft jumping robots.

Besides, due to the rolled structure, the actuator can also generate autonomously continuous rolling motion under light. This biomimetic actuator that integrating latch structure, precise energy control and release in a spatially efficient way not only provides a new strategy for the development of high-performance untethered jumping robots with highly controllable motion, but also reveals their application prospect in locomotion and miniaturized transportation.

2. Materials and methods

2.1. Materials

All reagents used in this paper were purchased from Shanghai Macklin Biochemical Co., Ltd. Prior to performing the synthesis of MXene, the Ti_3AlC_2 MAX phase powders were screened for large-size Ti_3AlC_2 particles. The Ti_3AlC_2 powders were placed in a beaker filled with water and stood for 15 min, and then separating the sediment and repeating the above steps for three times. After that, the obtained Ti_3AlC_2 powders were dried in a vacuum oven of 80°C and collected.

2.2. Synthesis of $\text{Ti}_3\text{C}_2\text{T}_x$ MXene

The $\text{Ti}_3\text{C}_2\text{T}_x$ MXene was synthesized by etching Ti_3AlC_2 MAX phase with HCl/LiF. The etching solution was prepared by dissolving 4 g of LiF into 50 mL of 9 M HCl. Then, 2 g of Ti_3AlC_2 powders were slowly added into the etching solution for about 5 min. The etching process continued for 30 h at 50°C under magnetic stirring. The reaction product was washed with DI water repeatedly until the pH value of supernatant reached 6–7. After that, the dispersion was shaken by hand for 30 min and then centrifuged at 1500 rpm for 30 min, and the MXene dispersion (the supernatant liquid) was collected.

2.3. Fabrication of MXene/PDMS bilayer composite film

The MXene dispersion (3 mg mL^{-1}) was dripped on the glass substrate ($10 \text{ mm} \times 27 \text{ mm}$) and covered the whole substrate surface. The dispersion was naturally dried in air for more than 48 h, forming a pure MXene layer on the substrate. After removing the air bubbles of PDMS mixture (which consisted of base agent and cure agent with a mass ratio of 10:1), the PDMS mixture was cast on the MXene layer through spin-coating technique. Then, the composite with glass substrate was placed in an oven at 100°C for 2 h to solidify the PDMS mixture and then the bilayer composite was cooled at room temperature. After that, a PI templet ($10 \text{ mm} \times 27 \text{ mm}$, and there is a size of $3 \text{ mm} \times 8 \text{ mm}$ rectangular hole near the edge) was covered on the surface of the cured PDMS layer, and then the uncured PDMS without cure agent was coated on the one edge of bilayer film by spin-coating method (the area density of the uncured PDMS is about 0.8 mg cm^{-2}). Finally, by removing the PI templet and peeling the bilayer off from the substrate, the MXene/PDMS bilayer composite with a closed rolled initial structure can be obtained.

2.4. Characterization

The morphology and structure of the MXene/PDMS bilayer composite were obtained by scanning electron microscopy (FESEM, model SU8000, Hitachi, Japan), transmission electron microscopy (JEM-2100 F, JEOL, Japan), and atomic force microscopy (NTEGRA, NT-MDT, Russia). The XRD pattern was performed on an X-ray diffractometer with high-intensity graphite monochromatized $\text{Cu K}\alpha$ radiation (Rigaku-TTR3, Japan). The stress-strain curve of the MXene film was obtained by a universal mechanical testing machine (5944, Instron, America). The temperature changes of the MXene/PDMS bilayer composite photoactuator under light irradiation was recorded by a thermographic high-resolution system (Fotric 225–1, America).

3. Results and discussion

3.1. Design, fabrication, and characterization of the closed rolled MXene/PDMS film

Jumping is an important movement mode of many organisms in nature. Although the muscle actuation power of many soft worm-like insect larvae is small, they can often achieve fast jumping movement

through different power-amplified strategies. The larva of gall midges is a typical example (Fig. 1a). In the jumping preparation process, it forms its body into a loop by latching its anterior and posterior, and then store elastic energy by pressurizing a part of the body to constrict the loop and form a transient ‘leg’ (inset of Fig. 1a). When the latch is opened, the stored elastic energy is released simultaneously, pushing the ‘leg’ against the ground and propelling the larva jump upward with rotation in the air. The actuation power amplification based on the latching

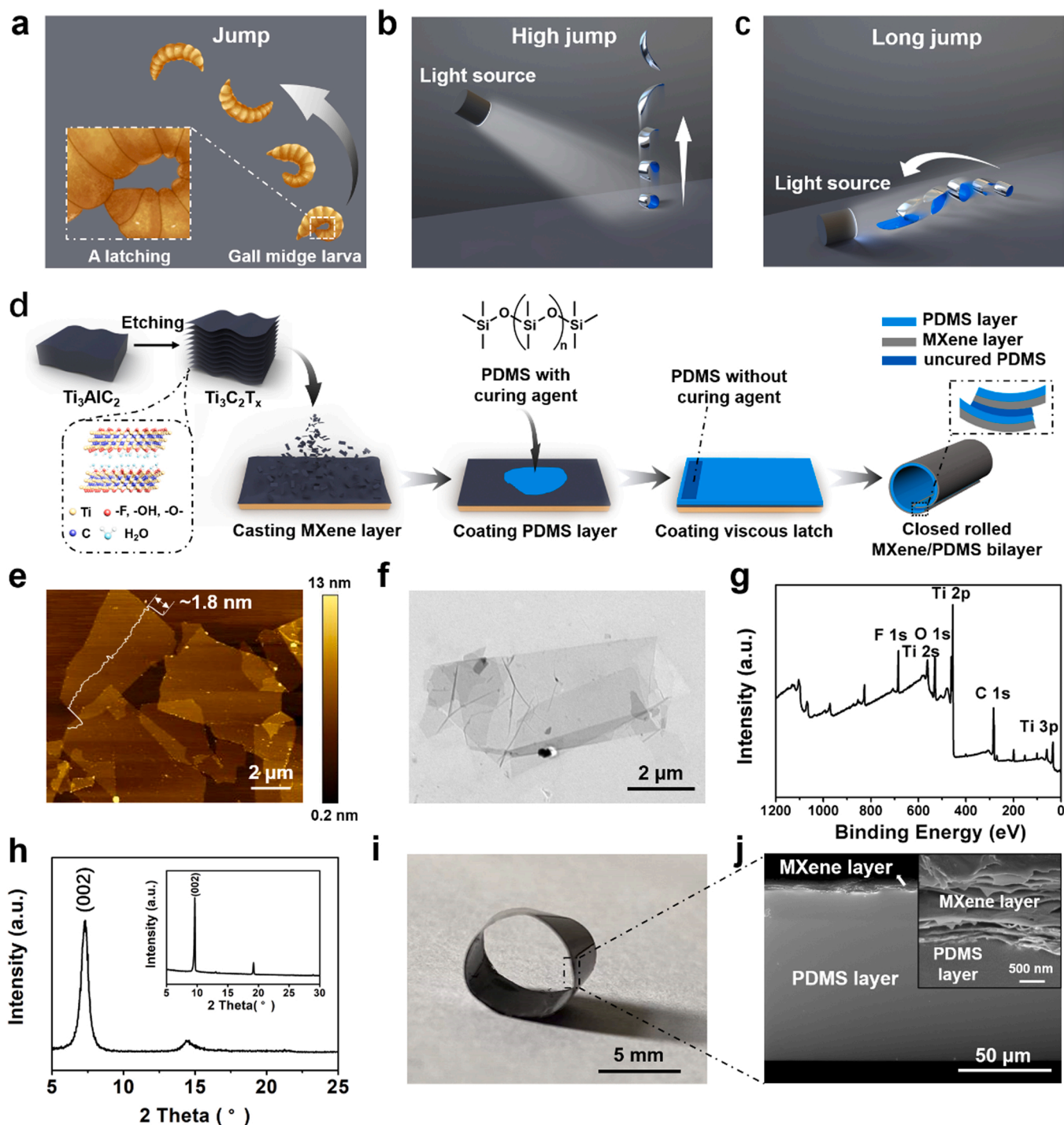


Fig. 1. Design, fabrication, and characterization of the closed rolled MXene/PDMS film. (a) Schematic diagram of the jumping process of the legless gall midge larva. (b) Schematic diagram of the high jump and (c) long jump of the untethered soft jumping actuator controlled by light. (d) Schematic illustration of the fabrication procedure of the closed rolled MXene/PDMS bilayer composite film. (e) AFM and (f) TEM image of the MXene nanosheets. (g) XPS spectra of the MXene nanosheets. (h) XRD pattern of the assembled MXene film. The inset is the XRD patterns of Ti_3AlC_2 MAX phase. (i) Optical image of the closed rolled MXene/PDMS film. (j) Cross-sectional SEM images of the MXene/PDMS film. The inset shows a magnified SEM image.

mechanism of gall midge larvae provides the inspiration for the development of biomimetic jumping actuators with long jump and high jump controlled by the irradiation angle of the light (Fig. 1b and c), which can completely simulate the jumping way of this gall midge larva.

Fig. 1d schematically shows the fabrication process of the closed rolled bilayer composite film. Here, we chose $\text{Ti}_3\text{C}_2\text{T}_x$ MXene nanosheets as the photoactive component to fabricate the biomimetic insect larva-like jumping actuator due to the excellent photothermal effect and thermal shrinkage property [38,43,44]. The polydimethylsiloxane (PDMS) is also chosen because of its remarkable mechanical elasticity and large thermal expansion mismatch with MXene [32,36]. Firstly, the MXene dispersion obtained by etching and delaminating the Ti_3AlC_2 MAX-phase with a mixture of HCl and LiF is cast onto a glass substrate and then dried in air to form a pure MXene film. Afterwards, PDMS layer is casted on the surface of the MXene film by spin coating method. The composite film is heated at 100 °C for 2 h to solidify the PDMS layer and then cooled at room temperature. After that, a pre-designed polyimide (PI) template is covered on the cured PDMS layer, and additional PDMS solution without curing is spin-coated on the template, forming a viscous region. Then, the template is removed and the composite film is peeled off from the substrate, obtaining the MXene/PDMS actuator with closed loop structure the same as the that of the gall midge larva before jumping.

The micromorphology of the MXene is characterized by atomic force microscopy (AFM) and transmission electron microscopy (TEM). The complete and clear MXene nanosheet with a thickness of ~ 1.8 nm is shown in AFM image in Fig. 1e. Fig. 1f shows the TEM image of the MXene nanosheets, further indicating the relatively larger size of the nanosheets. The X-ray photoelectron spectroscopy (XPS) of the $\text{Ti}_3\text{C}_2\text{T}_x$ MXene is also provided in Figs. 1g and S1. The existed oxygen elements mainly derive from the oxygen-containing functional groups on the surface of the MXene nanosheets. These oxygen-containing functional groups facilitate the adsorption of water molecules, which can lead to the reversible volume change of the assembled layered MXene film [40]. In order to investigate the layered microstructure, the X-ray diffraction (XRD) patterns of the MXene film is also measured (Fig. 1h). It can be seen the characteristic diffraction peak at 7.29° corresponds to the (002) lattice plane of MXene. According to Bragg's Equation, the *d-spacing* of the obtained layered MXene film is calculated to be about ~ 12.12 Å. The XRD patterns of Ti_3AlC_2 powder is also provided in the inset image for comparison. Fig. S2 shows the Raman spectrum of the MXene. The distinct sharp peak around 199 cm^{-1} represents out-of-plane (A_{1g}) vibrations of Ti, C, and O atoms. The region $225\text{--}480\text{ cm}^{-1}$ corresponds to in-plane (E_g) vibrations of surface groups attached to Ti atoms. The region $580\text{--}730\text{ cm}^{-1}$ is assigned mostly to both E_g and A_{1g} vibrations of C atoms, where the peaks around 717 cm^{-1} correspond to A_{1g} vibrations of C atoms. The assembled MXene film shows great mechanical performance. It can be seen from the stress-strain curve (Fig. S3) that the tensile strength can reach 44.5 MPa and the Young's modulus is about 4.8 GPa, which may be due to the relatively large size of the nanosheets in the layered structure film. Fig. 1i gives the optical image of the MXene/PDMS composite film, which clearly shows a closed loop shape. This unique rolled structure is attributed to the generated interfacial thermal stress from large thermal deformation mismatch between the MXene and PDMS. As we mentioned above, MXene film owns a reversible thermal shrinkage deformation, while PDMS has a large thermal expansion deformation. The large thermal deformation difference between MXene and PDMS leads to the generation of the interfacial thermal stress during high temperature curing process in the fabrication of MXene/PDMS film. After cooling down to room temperature, with the shrinkage of PDMS and expansion of MXene, the release of thermal stress causes the film to curl towards the PDMS side and form a loop. The existence of uncured PDMS can conglutinate the two ends of the rolled film, which serves as a latch to close the loop. Therefore, a closed rolled MXene/PDMS film is obtained. Fig. 1j gives the cross-sectional scanning electron microscopy (SEM) image of the MXene/PDMS film, which

clearly shows the bilayer structure. The inset magnified image further indicates the loosely lamellar structure of MXene and the tight bonding between the MXene and PDMS layers. From the top view SEM image (Fig. S4), the stacks of large size MXene nanosheets in MXene layer are further observed. It is worth noting that this MXene/PDMS bilayer film shows a great structural stability. As shown in Fig. S5, after 10,000 times of mechanical deformation, the MXene layer and the PDMS layer still remains a good combination without separation. In addition, as shown in Fig. S6, the contact angle of the MXene layer is about 48° , which indicates that the MXene layer has a great hydrophilicity.

3.2. Light-driven elastic deformation of the closed rolled actuator

The rolled MXene/PDMS film actuator can exhibit unique reversible large deformation from originally rolled state to flat state under light irradiation (Fig. 2a), which is mainly due to the excellent photothermal effect of MXene, thermal shrinkage of MXene from the adjustable interlayer spacing, and thermal expansion of PDMS. In order to investigate the important effect of the uncured PDMS as the latch on the release of light-driven actuation output, the unclosed rolled MXene/PDMS film actuator which has not been coated with uncured PDMS is also fabricated, and its light-driven actuation is also studied. As shown in Fig. 2b and Movie S1, the unclosed rolled actuator that is curled up to a complete loop but not closed unfolds to become flat state in 3 s when it is exposed to the light irradiation from the left side. After light is turned off, it curls up to the original rolled state. The infrared images of the unclosed MXene/PDMS actuator during the light-induced actuation process are given in Fig. S7. As we know, MXene nanosheets have excellent photothermal ability and high thermal conductivity. When the actuator is irradiated by light, the absorbed light energy in MXene layer is quickly converted into thermal energy, resulting in the fast temperature increase and large volume expansion of the PDMS layer. On the other hand, the oxygen-containing functional group on the surface of the MXene sheets can adsorb water molecules through hydrogen bonding, leading to the intercalation of water molecules inside the layered MXene film. Under light irradiation, the desorption and deintercalation of water molecules occurs in MXene layer due to the photothermal effect, which results in the decreases of interlayer *d-spacing* and the shrinkage deformation of MXene layer. Therefore, a combination of the thermal deformation mismatch between PDMS and MXene layers leads to the unfolding deformation of the rolled film. Moreover, in order to verify the actuation mechanism of this MXene/PDMS film actuator, thermogravimetric test on the MXene/PDMS film has been performed to analyze the water loss of this actuator (Fig. S8). When the temperature reaches to 100 °C, the mass loss of this film is about 1.98%. In addition, the real-time weight loss of this actuator with incident light on and off has also been recorded (Fig. S9). Similar to other MXene-based actuators, when the MXene/PDMS film is exposed to the light irradiation, the weight of the film decreases; when the light is removed, the weight of the film is recovered. These results further confirm the actuation mechanism related to the deintercalation/intercalation of water molecules. Fig. 2c shows the detailed deformation angle change and temperature variation of the unclosed MXene/PDMS actuator under light irradiation (300 mW cm^{-2}). The unclosed actuator reaches the deformation angle of 225° with the temperature increase after continuous irradiation for 3 s, and the average deformation speed is 75° s^{-1} . After turning off the light irradiation, the temperature of the actuator decreases and the actuator returns to its initial shape within 5 s. The light-driven actuation of the unclosed actuator with different light intensity is also shown in Fig. 2d. With the increase of the light intensity, both the deformation angle and temperature of this unclosed actuator increase linearly. It is worth noting that this MXene/PDMS film actuator with unclosed structure can also be actuated upon the sunlight irradiation, as shown in Fig. S10. The operation stability of the light-induced actuation is also examined, as shown in Fig. S11. During the 100 cycles light stimulation, the maximum deformation angle remains almost stable. In

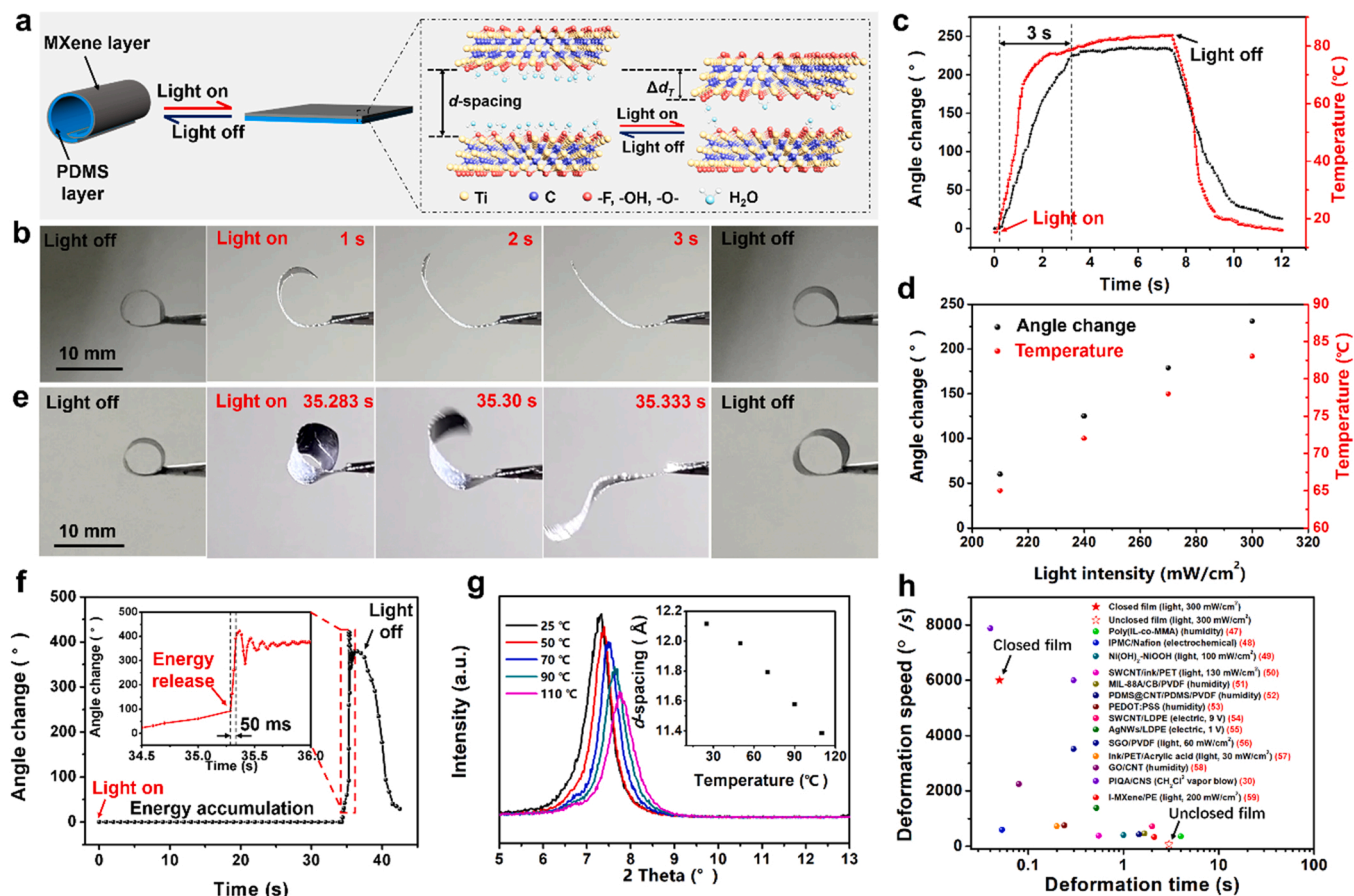


Fig. 2. Light-induced actuation of the rolled MXene/PDMS film. (a) Schematic illustration of the actuation behavior of the rolled MXene/PDMS film. (b) Optical images of the light-induced actuation of the unclosed MXene/PDMS film. (c) The detailed deformation angle changes and temperature variation of the unclosed MXene/PDMS film under the light irradiation. (d) Light-induced actuation of the unclosed MXene/PDMS film with different light intensity. (e) Optical images of the light-induced actuation of the closed MXene/PDMS film under light irradiation. (f) The detailed deformation angle changes of the closed MXene/PDMS film under light irradiation. The inset shows a magnified deformation process during the open of the latch. (g) Deformation speed/time comparison of the MXene/PDMS film with that of the other reported film actuators. (h) XRD patterns of the MXene film under different temperatures. The inset is the calculated interlayer d -spacing of the MXene under different temperatures [47–59].

addition to the light-induced actuation behavior of this MXene/PDMS film actuator, the thermal-induced and electric-induced actuation behavior of this actuator has also been given in the [Supplementary Materials](#) (Figs. S12 and S13).

Supplementary material related to this article can be found online at [doi:10.1016/j.nanoen.2022.107848](https://doi.org/10.1016/j.nanoen.2022.107848).

The gall midge larvae realize jumping motion by latching anterior and posterior to form a closed loop. Here, uncured PDMS is used as an adhesive latch to conglutinate the two ends of the unclosed rolled MXene/PDMS film, obtaining the closed loop. Unlike the unclosed actuator, the closed film does not unfold immediately under the light irradiation, but produces ultra-fast deformation behavior after a period of light irradiation. This involves the storage, accumulation, and instantaneous release of elastic mechanical energy through the latch in closed rolled actuator. As shown in [Fig. 2e](#) and [Movie S2](#), after continuous light irradiation for the 35 s (300 mW cm^{-2}), the closed MXene/PDMS film still keeps the closed rolled state. Although there is a slight slippage on the two ends of the film, the closed loop is still remained due to the operation of the adhesive latch for preventing the light-driven deformation. During this process, because of the action of the adhesive latch, a large amount of light-driven elastic mechanical energy is stored and accumulated in the film. The infrared thermal images of the closed MXene/PDMS film under light irradiation is also given in [Fig. S14](#). It can be seen that the temperature of the closed film continuously increases during the irradiation, which means the

continuous storage of energy. As light irradiation continues, when the energy accumulated in the film reaches a critical point, the latch is open to suddenly release the elastic energy. Consequently, the film unfolds instantaneously and produces angle change of more than 300° in only 50 ms ([Fig. 2f](#)). In the deformation process, the deformation speed of the MXene/PDMS film can reach as high as $6000^\circ \text{ s}^{-1}$. Moreover, for the purpose of verifying the thermal shrinkage of the MXene film from the interlayer spacing change, the XRD patterns of the MXene film under different temperatures is measured, as shown in [Fig. 2g](#). With the increase of temperature, the (002) diffraction peak is shifted to the right, indicating the decrease of the interlayer d -spacing of the MXene. The detailed interlayer d -spacing of the MXene under different temperatures are also calculated by Bragg's Equation and shown in the inset of [Fig. 2g](#). When the temperature increases from 25°C to 110°C , the d -spacing decreases from 12.12 \AA to 11.38 \AA . We also compare the deformation performance of the closed actuator with the unclosed actuator and that of the other reported soft actuators ([Fig. 2h](#)). The closed rolled MXene/PDMS actuator exhibits outstanding performance in terms of deformation speed in the photoactuators.

Supplementary material related to this article can be found online at [doi:10.1016/j.nanoen.2022.107848](https://doi.org/10.1016/j.nanoen.2022.107848).

3.3. High jump motion of the untethered jumping actuator under light

Based on the instantaneous energy release of the closed rolled

MXene/PDMS film due to the adhesive latch, we have designed and fabricated a biomimetic untethered soft jumping actuator by simulating the latching mechanism of the gall midge larvae. As shown in Fig. S15, this jumping actuator is simply fabricated by tailoring the two edges of the MXene/PDMS film (MXene layer thickness is $\sim 4 \mu\text{m}$, PDMS layer thickness is $\sim 93 \mu\text{m}$) into the triangle shape before peeled the film off from the substrate. The jumping mode of the actuator can be precisely controlled by adjusting the irradiation angle. When selectively irradiating the local area of the jumping actuator, the light-induced deformation of the irradiated site leads to a change in the direction of the force applied on the ground by the actuator, resulting in different jumping modes such as high jump or long jump. When placed on the ground, the jumping actuator can produce vertical high jumping motion under the light irradiation from the left with an irradiation angle of 30° (Fig. 3a). The detailed light-powered high jump process with different time is shown in Fig. 3b and Movie S3, where Δt is the time elapsed since the actuator take-off. When exposed to the light irradiation (intensity of 360 mW cm^{-2} , and irradiation angle of 30°) from the upper left, the actuator stays in place for a period of time (about 30 s), then suddenly jumps vertically, flips in the air, and falls to the ground. This light-powered high jump process is further analyzed, as shown in Fig. 3c. In

the initial state, the two edges (part 'I' and part 'III') of the jumping actuator are tightly bound by the uncured PDMS adhesive. When the actuator is illuminated by continuous light from the upper left, irradiated site part 'II' starts to produce light-induced driving deformation and affects other parts of the actuator, so that part 'III' is subjected to the force F applied by the other parts of the actuator. F can be decomposed into vertical downward force F_1 and horizontal rightward force F_2 . The existence of F_2 causes part 'III' to have a tendency to move to the right. This causes part 'I', which is in contact with part 'III', to exert a leftward static friction force f on part 'III'. In addition, part 'III' is also subjected to gravity G and the supporting force N of part 'I'. Before f reaches the maximum static friction f_{max} , part 'III' remains stationary under the combined force of F , f , G and N . With the continuous illumination, the strain energy stored in the actuator increases gradually, which also causes the force F_2 acting on part 'III' by the other parts of the actuator to gradually increase. When $F_2 > f_{\text{max}}$, the relative sliding occurs between part 'I' and part 'III', and the energy accumulation stage of the actuator ends. The actuator then enters the energy release stage. In this stage, the actuator is mainly subjected to two forces: gravity G' , the supporting force N' exerted by the ground. Under the action of the supporting force N' , the actuator produces an upward acceleration a_y , so that the MXene/PDMS

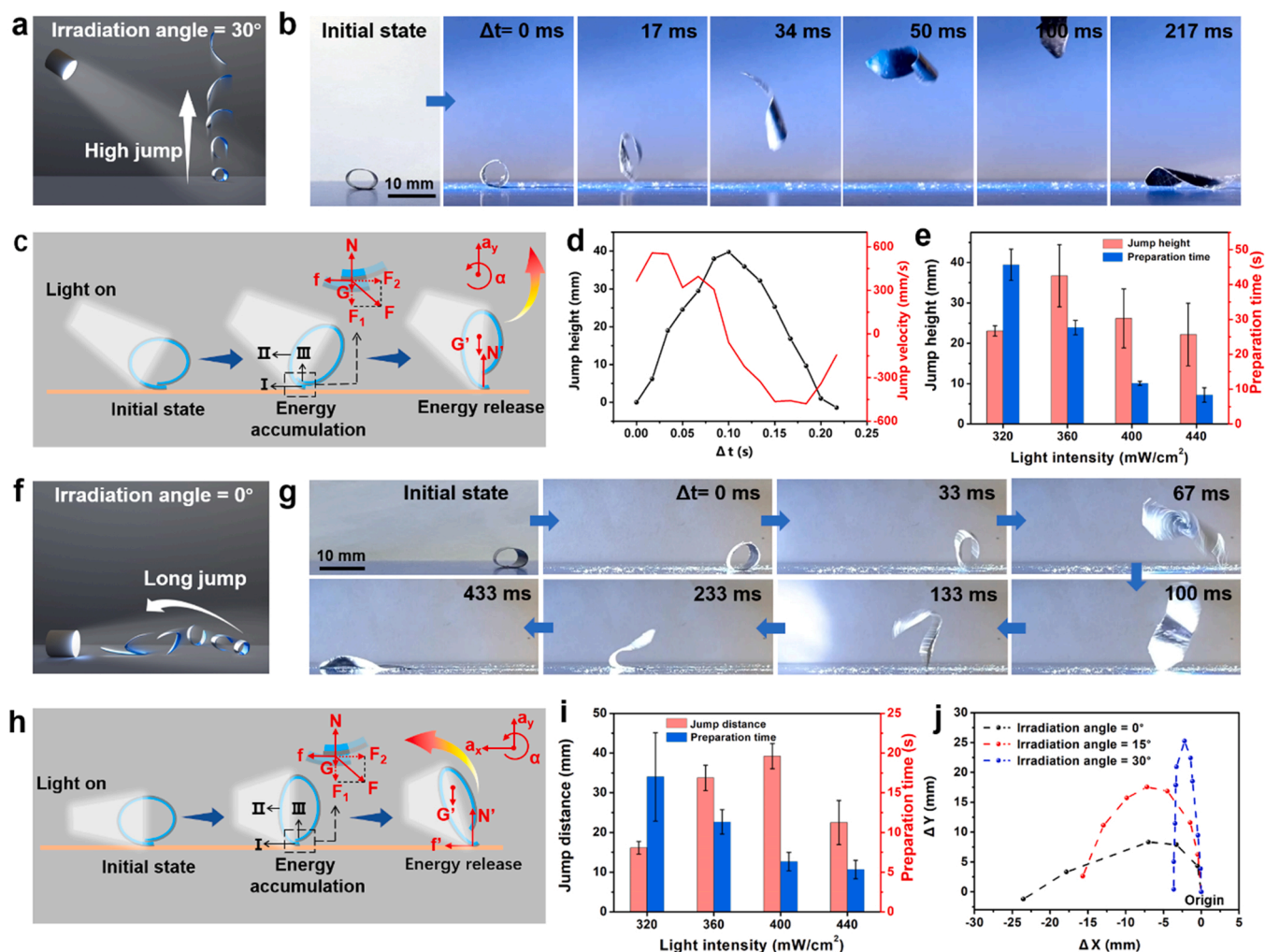


Fig. 3. Controllable jumping motion powered and regulated by light. (a) Schematic diagram of the light-powered high jump process of the MXene/PDMS jumping actuator. (b) Optical images of the high jump process under light with irradiation angle of 30° with different time. (c) The force analysis of the jumping actuator in the high jump process. (d) Jump height and velocity of the jumping actuator versus time in the high jump process. (e) High jump performance of the jumping actuator under light irradiation with different light intensity. (f) Schematic diagram of the light-powered long jump process of the MXene/PDMS jumping actuator. (g) Optical images of the long jump process under light with irradiation angle of 0° with different time. (h) The force analysis of the jumping actuator in the long jump process. (i) Long jump performance of the jumping actuator under light irradiation with different light intensity. (j) The typical jumping trajectory of the center of mass of the actuator illuminated by continuous light with different irradiation angle.

PDMS untethered soft actuator can realize the high jump motion. The actuator's gravity G' and the ground's supporting force N' are not on the same action line, resulting in angular acceleration α , which eventually causes the actuator to rotate in the air. Fig. 3d shows the jump height and velocity of the MXene/PDMS jumping actuator in the high jump process. The actuator can attain a maximum height of 41 mm (10.3 times of its body height) in 100 ms and the whole high jump process utilized 217 ms. The initial velocity of the soft untethered jump actuator can attain 0.56 m s^{-1} . Based on the height change of the center of gravity ($\Delta H \approx 30 \text{ mm}$) and the mass ($m \approx 19 \text{ mg}$) of the actuator, the output energy ($\Delta E = mg\Delta H$, where g is the gravitational acceleration) and the specific work density are calculated to be about $5.59 \text{ }\mu\text{J}$ and 0.29 J kg^{-1} , respectively. The high jump performance of this actuator under light irradiation with different light intensity is also studied (irradiation angle of 30°), as shown in Fig. 3e. The energy stored by the actuator under light irradiation is related to the light intensity and irradiation time. With the enhancement of light intensity, the preparation time before the actuator take-off gradually decreases. The optimal high jump height of this jumping actuator is obtained when the light intensity is 360 mW cm^{-2} .

Supplementary material related to this article can be found online at [doi:10.1016/j.nanoen.2022.107848](https://doi.org/10.1016/j.nanoen.2022.107848).

3.4. Long jump motion of the untethered jumping actuator under light

Besides the high jump motion, the actuator can also produce horizontal long jump motion when it is illuminated by light from the left with an irradiation angle of 0° (Fig. 3f). As shown in Fig. 3g and Movie S4, under the horizontal light irradiation (intensity of 400 mW cm^{-2} , and irradiation angle of 0°) from the left, the actuator produces long jump motion to the left side. Fig. S16 shows the jump distance of the actuator versus time in the long jump process. The actuator can attain a maximum horizontal jump distance of 40 mm which is 5.7 times its body length. In order to investigate the mechanism of the long jump powered by the horizontal irradiated light, the force analysis of the actuator is also conducted, as shown in Fig. 3h. In addition to the upward acceleration a_y and angular acceleration α of the actuator, the lower irradiation angle causes the other parts of the actuator to exert a greater horizontal component force on the part 'I'. This lead to the tendency of part 'I' to slide to the right, so that the actuator is subjected to the leftward friction f exerted by the ground. Under the action of f , the actuator produces an acceleration a_x to the left. Under the combined action of a_x , a_y , and α , the long jump motion can be realized. Moreover, the long jump performance of the actuator under light irradiation with different light intensity is also provided (Fig. 3i). Similar to that of the high jump, as the light intensity increases, the preparation time of the actuator before jumping decreases gradually. When the light intensity is 400 mW cm^{-2} , the jumping actuator can obtain the optimal long jump distance. In addition to the vertical high jump and horizontal long jump motion, the jumping motion with different jumping angle can also be achieved by adjusting the irradiation angle of the light (Fig. S17). For example, when the light (intensity of 360 mW cm^{-2}) is irradiated with angle of 15° , the jumping actuator can produce a parabolic jumping motion towards the oblique direction, as shown in Fig. S17a. Meanwhile, under the condition of keeping light intensity while changing the irradiation angle (30° and 0°), the high jump and long jump are realized, respectively (Fig. S17b and c). The trajectories of these different light-driven jumping motion illuminated under different irradiation angles (0° , 15° , and 30°) are given in Fig. 3j. Here, in order to clearly reveal the trend of jumping motion, we equivalent the actuator to the center of mass and neglect its rotation motion. In this trajectory, ΔX and ΔY represent the distance and height that the center of mass of the jumping actuator moves along the horizontal and vertical directions respectively, and the negative value of ΔX means that the actuator moves to the left side. This further clarifies the precise regulation of the jumping motion by adjusting the external light irradiation.

Supplementary material related to this article can be found online at [doi:10.1016/j.nanoen.2022.107848](https://doi.org/10.1016/j.nanoen.2022.107848).

3.5. Jumping with a load

More importantly, this jumping actuator can also achieve jumping motion with a load, which has never been realized in the current untethered soft jumping robots. As shown in Fig. 4a and Movie S5, when a $\sim 10 \text{ mg}$ object is fixed inside the MXene/PDMS actuator ($\sim 19 \text{ mg}$), it can carry this load to realize high jump motion under light irradiation (light intensity of 360 mW cm^{-2} , and irradiation angle of 30°). The detailed jump height change of the actuator with load with different time is also given in Fig. S18. It can be seen that the actuator can carry the load to jump to a maximum height of 33.4 mm (the height change of the center of gravity $\Delta H \approx 26 \text{ mm}$) in 83 ms, which is 8.4 times actuator's body height. By calculation, the output energy is $7.39 \text{ }\mu\text{J}$ and the specific work density is 0.25 J kg^{-1} , respectively.

Supplementary material related to this article can be found online at [doi:10.1016/j.nanoen.2022.107848](https://doi.org/10.1016/j.nanoen.2022.107848).

In addition to the light intensity and irradiation angle, the stickiness of the latch, thickness of the MXene and PDMS layers, and the geometry dimension of the actuator also have a great impact on the jumping performance of the MXene/PDMS jumping actuator. For this MXene/PDMS actuator, if the adhesion of latch is too small, the energy that can be stored by the actuator under light irradiation will be very small, which will not be enough to make the actuator achieve jump movement; if the adhesion of latch is too large, the closed latch cannot be opened under light irradiation, and the jump movement also cannot be realized. According to our tests, when the light intensity is 360 mW cm^{-2} , and the area density of the uncured PDMS latch is $0.3\text{--}1.5 \text{ mg cm}^{-2}$, the actuator can produce jumping movement. The thickness of MXene and PDMS layers can affect the initial curvature of the actuator, which will affect the jumping performance of the actuator (Fig. S19). With the increase of the thickness of the MXene layer or the PDMS layer, the initial curvature of the film decreases, which reducing the contact area between the uncured PDMS latch and the MXene layer, so that the stored energy of the actuator under light irradiation reduces, thus reducing the jump performance. If the initial curvature of the actuator is too small, an effective latch structure cannot be formed, so the actuator cannot produce jumping motion. The geometric dimension of the actuator also can affect the contact area between the latch and the MXene layer, which will further affect the jumping performance of the actuator. If the contact area between the latch and MXene layer is too large, the latch structure will be hard to open, and the jumping motion cannot be realized. That is why the two ends of the actuator were designed into a triangle shape.

The comparison of jumping performance of this jumping actuator with that of the other soft actuators are also provided in Fig. 4b, c, and Table S1, which confirms that our jumping actuator has a good controllability. The jumping performance in a single direction of this MXene/PDMS jumping actuator may not be so superior over some particular jumping actuators, but it enables precise and controllable jump motions in different directions, which is difficult to achieve by the other jumping actuators. There are some ways can be considered to further improve the jumping ability of the actuator. For example, incorporating structurally nonlinear mechanism such as snap-through to enhance the jumping performance of the actuator. Besides, the storage of elastic energy can be improved by designing some bistable structures combining soft and hard segments, and the energy accumulation time can be improved by designing some anchored microstructures at the latch of the actuator, thus improving the jumping ability of the actuator.

3.6. Rolling motion of the actuator under light

Due to the unique rolled structure, a rolling actuator capable of autonomously continuous rolling under continuous light irradiation is

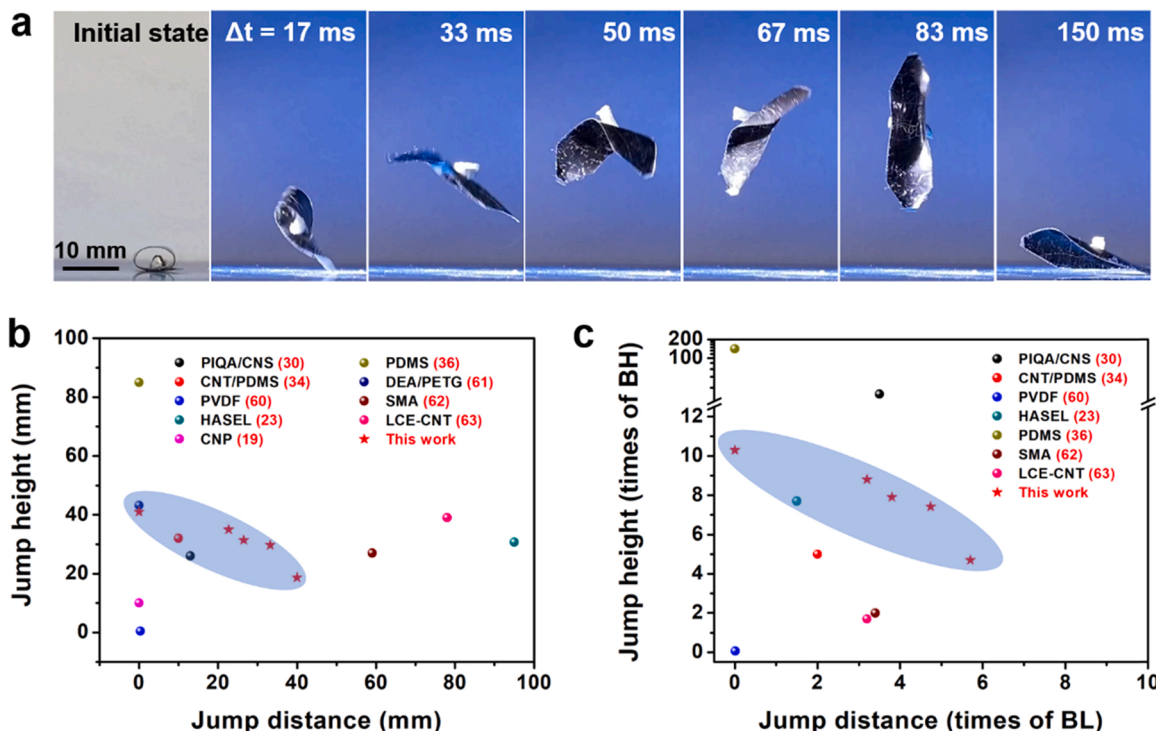


Fig. 4. Jumping motion with a load and jump performance comparison. (a) Optical images of the jumping actuator carrying a load to jump high. (b, c) Comparison of jumping performance of the actuator (jump height and jump distance) with that of the other reported soft actuators. Here BH and BL stand for the body height and body length of the actuator, respectively [60–63].

also designed. A PI tape is used to fix the joint of the two edges of the unclosed rolled MXene/PDMS film, forming the circular shaped rolling actuator (Fig. S20). Fig. 5a schematically shows the light-induced rolling process of this MXene/PDMS rolling actuator. The rolling motion is attributed to the constant change of the center of gravity of the circular actuator under continuous light irradiation. As illustrated in Fig. 5b, the circular actuator is placed on a horizontal ground, and the center of gravity of the actuator is at the center of the circle without light irradiation. When the actuator is illuminated by light from the left side, the light-induced driving deformation can be realized in the sunny side of the actuator. At the same time, the deformation of the shaded side without direct light irradiation is much smaller. The asymmetric

deformation leads to the changes of the position of the actuator’s center of gravity, which can generate torque between the actuator and the ground and result in the rolling motion of the actuator to the right. The above process circulates under continuous light irradiation, so that the circular actuator can move continuously and autonomously away from the light source. Fig. 5c and Movie S6 show the light-induced rolling process of the circular actuator at different times (light intensity of 360 mW cm⁻²). This actuator can roll more than 83 mm in 6.6 s, and the average rolling speed is about 12.6 mm s⁻¹. The detailed rolling distance changes versus irradiation time is also given in Fig. S21.

Supplementary material related to this article can be found online at [doi:10.1016/j.nanoen.2022.107848](https://doi.org/10.1016/j.nanoen.2022.107848).

4. Conclusions

Inspired by the jumping process of gall midge larvae involving the latching mechanism, we have designed and fabricated a MXene-based untethered soft jumping actuator with a closed loop structure containing the adhesive latch, which is the same as shape of gall midge larvae before jumping. This actuator generates jumping motion under light irradiation, which is mainly attributed to the light-driven deformation of MXene composite film, the good elasticity of loop structure, and the storage and instantaneous release of elastic deformation energy caused by the action of latch. Moreover, the regulation of jumping mode (e.g., vertical high jump or horizontal long jump) can also be realized by simply adjusting the light irradiation angle. The maximum jump height can reach more than 41 mm that is 10.3 times its own height. More importantly, this actuator can jump with loading (0.5 times its own weight) under light. Besides the jumping motion, the actuator also realizes autonomously continuous rolling motion under light irradiation. This MXene-based biomimetic actuator provides a new sight for the development of next generation intelligent soft actuators and robots.

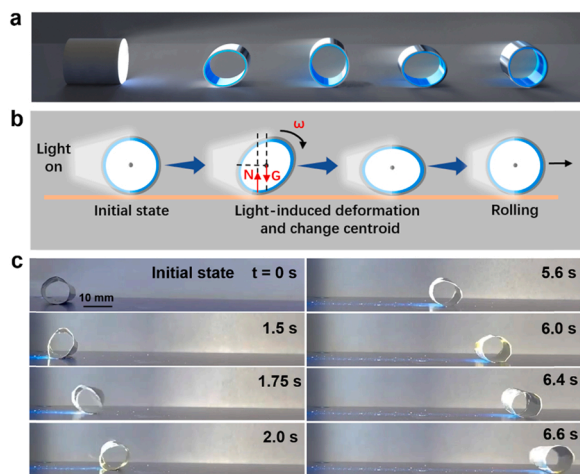


Fig. 5. Rolling motion of the MXene/PDMS circular actuator. (a) Schematic diagram of the rolling process of the rolling actuator powered by light. (b) The rolling mechanism of the circular actuator. (c) Optical images of the light-induced rolling process at different times.

CRediT authorship contribution statement

Liangliang Xu: Conceptualization, Methodology, Validation, Investigation, Data curation, Writing – original draft, Visualization. **Fuhua Xue:** Methodology, Formal analysis, Investigation, Writing – original draft. **Haowen Zheng:** Methodology, Investigation. **Qixiao Ji:** Formal analysis. **Changwen Qiu:** Investigation. **Zhong Chen:** Investigation. **Xu Zhao:** Validation. **Pengyang Li:** Investigation. **Ying Hu:** Writing – review & editing, Data curation. **Qingyu Peng:** Writing – review & editing, Project administration, Funding acquisition. **Xiaodong He:** Writing – review & editing, Project administration, Funding acquisition.

Author contributions

L. Xu, F. Xue, and H. Zheng contributed equally to this work. L. Xu, Y. Hu, Q. Peng, and X. He conceived the concepts and designed the research; H. Zheng and X. Zhao performed the fabrication of large size MXene dispersion; L. Xu, H. Zheng, and Q. Ji performed the fabrication of the bilayer composite film; L. Xu, Q. Ji, C. Qiu, and Z. Chen performed the characterizations and actuation behavior demonstrations; F. Xue and P. Li analyzed the jumping dynamics; L. Xu, Y. Hu, Q. Peng, and X. He wrote the paper. All authors discussed the results and commented on the manuscript.

Declaration of Competing Interest

The authors declare that they have no known competing financial interests or personal relationships that could have appeared to influence the work reported in this paper.

Data availability

No data was used for the research described in the article.

Acknowledgments

This work was supported by the Fundamental Research Funds for the Central Universities, Natural Science Foundation of Heilongjiang Province of China (Grant No. YQ2020E009), and National Key Laboratory of Science and Technology on Advanced Composites in Special Environments, Harbin Institute of Technology (KL.PYJH.2017.004, 6142905202907).

Appendix A. Supplementary material

Supplementary data associated with this article can be found in the online version at [doi:10.1016/j.nanoen.2022.107848](https://doi.org/10.1016/j.nanoen.2022.107848).

References

- D.P. Maitland, Locomotion by jumping in the Mediterranean fruit-fly larva *Ceratitis capitata*, *Nature* 355 (1992) 159–161, <https://doi.org/10.1038/355159a0>.
- G.M. Farley, M.J. Wise, J.S. Harrison, G.P. Sutton, C. Kuo, S.N. Patek, Adhesive latching and legless leaping in small, worm-like insect larvae, *J. Exp. Biol.* 222 (2019), <https://doi.org/10.1242/jeb.201129>.
- C. Gottler, K. Elflein, R. Siegart, M. Sitti, Spider origami: folding principle of jumping spider leg joints for bioinspired fluidic actuators, *Adv. Sci.* 8 (2021), 2003890, <https://doi.org/10.1002/adv.202003890>.
- E.H. David, *The jumping behavior of jumping spiders: a review*, *Peckhamia* 167 (2018).
- J.F.K. Campbell, H.K. Harry, How and why a parasitic nematode jumps, *Nature* 397 (1999) 485–486, <https://doi.org/10.1038/17254>.
- F. Rubio, F. Valero, C. Llopis-Albert, A review of mobile robots: concepts, methods, theoretical framework, and applications, *Int. J. Adv. Robot. Syst.* 16 (2019), <https://doi.org/10.1177/1729881419839596>.
- W. Hu, G.Z. Lum, M. Mastrangeli, M. Sitti, Small-scale soft-bodied robot with multimodal locomotion, *Nature* 554 (2018) 81–85, <https://doi.org/10.1038/nature25443>.
- W.B. Nicholas, T.T. Michael, T.B.O. Johannes, C.W. James, M. Bobak, B. Katia, M. W. George, J.W. Robert, A 3D-printed, functionally graded soft robot powered by combustion, *Science* 349 (2015) 161–165, <https://doi.org/10.1126/science.aab0129>.
- E.W. Hawkes, C. Xiao, R.A. Pelloquin, C. Keeley, M.R. Begley, M.T. Pope, M. Niemeier, Engineered jumpers overcome biological limits via work multiplication, *Nature* 604 (2022) 657–661, <https://doi.org/10.1038/s41586-022-04606-3>.
- S.J. Longo, S.M. Cox, E. Azizi, M. Ilton, J.P. Olberding, R. St Pierre, S.N. Patek, Beyond power amplification: latch-mediated spring actuation is an emerging framework for the study of diverse elastic systems, *J. Exp. Biol.* 222 (2019), <https://doi.org/10.1242/jeb.197889>.
- X.Q. Wang, G.W. Ho, Design of untethered soft material micromachine for life-like locomotion, *Mater. Today* 53 (2022) 197–216, <https://doi.org/10.1016/j.mat.2022.01.014>.
- M. Ilton, M.S. Bhamla, X. Ma, S.M. Cox, L.L. Fitchett, Y. Kim, J.S. Koh, D. Krishnamurthy, C.Y. Kuo, F.Z. Temel, et al., The principles of cascading power limits in small, fast biological and engineered systems, *Science* 360 (2018), <https://doi.org/10.1126/science.aao1082>.
- E. Siefert, E. Reysat, J. Bico, B. Roman, Bio-inspired pneumatic shape-morphing elastomers, *Nat. Mater.* 18 (2019) 24–28, <https://doi.org/10.1038/s41563-018-0219-x>.
- S.M. Mirvakili, I.W. Hunter, Artificial muscles: mechanisms, applications, and challenges, *Adv. Mater.* 30 (2018), <https://doi.org/10.1002/adma.201704407>.
- Y. Dong, L. Wang, N. Xia, Y. Wang, S. Wang, Z. Yang, D. Jin, X. Du, E. Yu, C. Pan, B. Liu, L. Zhang, Multi-stimuli-response programmable soft actuators with site-specific and anisotropic deformation behavior, *Nano Energy* 88 (2021), 106254, <https://doi.org/10.1016/j.nanoen.2021.106254>.
- X. Jin, Y. Shi, Z. Yuan, X. Huo, Z. Wu, Z. Wang, Bio-inspired soft actuator with contact feedback based on photothermal effect and triboelectric nanogenerator, *Nano Energy* 99 (2022), 107366, <https://doi.org/10.1016/j.nanoen.2022.107366>.
- S. Wang, Y. Gao, A. Wei, P. Xiao, Y. Liang, W. Lu, C. Chen, C. Zhang, G. Yang, H. Yao, T. Chen, Asymmetric elastoplasticity of stacked graphene assembly actualizes programmable untethered soft robotics, *Nat. Commun.* 11 (2020) 4359, <https://doi.org/10.1038/s41467-020-18214-0>.
- X. Qian, Y. Zhao, Y. Alsaied, X. Wang, M. Hua, T. Galy, H. Gopalakrishna, Y. Yang, J. Cui, N. Liu, M. Marszewski, L. Pilon, H. Jiang, X. He, Artificial phototropism for omnidirectional tracking and harvesting of light, *Nat. Nanotechnol.* 14 (2019) 1048–1055, <https://doi.org/10.1038/s41565-019-0562-3>.
- H. Arazoe, D. Miyajima, K. Akaike, F. Araoka, E. Sato, T. Hikima, M. Kawamoto, T. Aida, An autonomous actuator driven by fluctuations in ambient humidity, *Nat. Mater.* 15 (2016) 1084–1089, <https://doi.org/10.1038/NMAT4693>.
- Y. Chen, J. Yang, X. Zhang, Y. Feng, H. Zeng, L. Wang, W. Feng, Light-driven bimorph soft actuators: design, fabrication, and properties, *Mater. Horiz.* 8 (2021) 728–757, <https://doi.org/10.1039/d0mh01406k>.
- P. Lv, X. Yang, H.K. Bisoyi, H. Zeng, X. Zhang, Y. Chen, P. Xue, S. Shi, A. Priimagi, L. Wang, W. Feng, Q. Li, Stimulus-driven liquid metal and liquid crystal network actuators for programmable soft robotics, *Mater. Horiz.* 8 (2021) 2475–2484, <https://doi.org/10.1039/d1mh00623a>.
- X. Yang, Y. Chen, X. Zhang, P. Xue, P. Lv, Y. Yang, L. Wang, W. Feng, Bioinspired light-fueled water-walking soft robots based on liquid crystal network actuators with polymerizable miniaturized gold nanorods, *Nano Today* 43 (2022), 101419, <https://doi.org/10.1016/j.nantod.2022.101419>.
- R. Chen, Z. Yuan, J. Guo, L. Bai, X. Zhu, F. Liu, H. Pu, L. Xin, Y. Peng, J. Luo, L. Wen, Y. Sun, Legless soft robots capable of rapid, continuous, and steered jumping, *Nat. Commun.* 12 (2021) 7028, <https://doi.org/10.1038/s41467-021-27265-w>.
- W. Sun, B. Li, F. Zhang, C. Fang, Y. Lu, X. Gao, C. Cao, G. Chen, C. Zhang, Z. Wang, TENG-bot: triboelectric nanogenerator powered soft robot made of uni-directional dielectric elastomer, *Nano Energy* 85 (2021), 106012, <https://doi.org/10.1016/j.nanoen.2021.106012>.
- X. Chen, Y. Wu, A. Yu, L. Xu, L. Zheng, Y. Liu, H. Li, Z. Wang, Self-powered modulation of elastomeric optical grating by using triboelectric nanogenerator, *Nano Energy* 38 (2017) 91–100, <https://doi.org/10.1016/j.nanoen.2017.05.039>.
- B. Mishra, S. Sharma, Shape memory materials with reversible shape change and self-healing abilities: a review, *Mater. Today Proc.* 44 (2021) 4563–4568, <https://doi.org/10.1016/j.matpr.2020.10.820>.
- S. Namathoti, Rk V.M, R.S. P.S, A review on progress in magnetic, microwave, ultrasonic responsive shape-memory polymer composites, *Mater. Today Proc.* 56 (2022) 1182, <https://doi.org/10.1016/j.matpr.2021.11.151>.
- J. Yang, X. Zhang, X. Zhang, L. Wang, W. Feng, Q. Li, Beyond the visible: bioinspired infrared adaptive materials, *Adv. Mater.* 33 (2021), 2004754, <https://doi.org/10.1002/adma.202004754>.
- J. Ma, Y. Yang, C. Valenzuela, X. Zhang, L. Wang, W. Feng, Mechanochromic, shape-programmable and self-healable cholesteric liquid crystal elastomers enabled by dynamic covalent boronic ester bonds, *Angew. Chem. Int. Ed.* 60 (2021) 3390–3396, <https://doi.org/10.1002/ange.202116219>.
- K. Yu, X. Ji, T. Yuan, Y. Cheng, J. Li, X. Hu, Z. Liu, X. Zhou, L. Fang, Robust jumping actuator with a shrimp-shell architecture, *Adv. Mater.* 33 (2021), e2104558, <https://doi.org/10.1002/adma.202104558>.
- Z.Q. Zhao, J.W. Dunlop, X. Qiu, F. Huang, Z. Zhang, J. Heyda, J. Dzubielia, M. Antonietti, J. Yuan, An instant multi-responsive porous polymer actuator driven by solvent molecule sorption, *Nat. Commun.* 5 (2014) 4293, <https://doi.org/10.1038/ncomms5293>.

- [32] Y. Hu, Z. Li, T. Lan, W. Chen, Photoactuators for direct optical-to-mechanical energy conversion: from nanocomponent assembly to macroscopic deformation, *Adv. Mater.* 28 (2016) 10548–10556, <https://doi.org/10.1002/adma.201602685>.
- [33] T. Vasileiadis, T. Marchesi D'Alvise, C.M. Saak, M. Pochylski, S. Harvey, C. V. Synatschke, J. Gapsinski, G. Fytas, E.H.G. Backus, T. Weil, B. Graczykowski, Fast light-driven motion of polydopamine nanomembranes, *Nano Lett.* 22 (2022) 578–585, <https://doi.org/10.1021/acs.nanolett.1c03165>.
- [34] Y. Hu, J. Liu, L. Chang, L. Yang, A. Xu, K. Qi, P. Lu, G. Wu, W. Chen, Y. Wu, Electrically and sunlight-driven actuator with versatile biomimetic motions based on rolled carbon nanotube bilayer composite, *Adv. Funct. Mater.* 27 (2017), <https://doi.org/10.1002/adfm.201704388>.
- [35] M. Li, X. Wang, B. Dong, M. Sitti, In-air fast response and high speed jumping and rolling of a light-driven hydrogel actuator, *Nat. Commun.* 11 (2020) 3988, <https://doi.org/10.1038/s41467-020-17775-4>.
- [36] Y. Kim, J. van den Berg, A.J. Crosby, Autonomous snapping and jumping polymer gels, *Nat. Mater.* 20 (2021) 1695–1701, <https://doi.org/10.1038/s41563-020-00909-w>.
- [37] H. Guo, A. Priimagi, H. Zeng, Optically controlled latching and launching in soft actuators, *Adv. Funct. Mater.* (2021), 2108919, <https://doi.org/10.1002/adfm.202108919>.
- [38] C. Wang, Y. Wang, X. Jiang, J. Xu, W. Huang, F. Zhang, J. Liu, F. Yang, Y. Song, Y. Ge, Q. Wu, M. Zhang, H. Chen, J. Liu, H. Zhang, MXene $Ti_3C_2T_x$: a promising photothermal conversion material and application in all-optical modulation and all-optical information loading, *Adv. Opt. Mater.* 7 (2019), <https://doi.org/10.1002/adom.201900060>.
- [39] K. Hantanasirisakul, Y. Gogotsi, Electronic and optical properties of 2D transition metal carbides and nitrides (MXenes), *Adv. Mater.* 30 (2018), e1804779, <https://doi.org/10.1002/adma.201804779>.
- [40] D. Xu, Z. Li, L. Li, J. Wang, Insights into the photothermal conversion of 2D MXene nanomaterials: synthesis, mechanism, and applications, *Adv. Funct. Mater.* 30 (2020), <https://doi.org/10.1002/adfm.202000712>.
- [41] S. Umrao, R. Tabassian, J. Kim, V.H. Nguyen, Q. Zhou, S. Nam, I.-K. Oh, MXene artificial muscles based on ionically cross-linked $Ti_3C_2T_x$ electrode for kinetic soft robotics, *Sci. Robot.* 4 (2019), <https://doi.org/10.1126/scirobotics.aaw7797>.
- [42] H. Zhao, R. Hu, P. Li, A. Gao, X. Sun, X. Zhang, X. Qi, Q. Fan, Y. Liu, X. Liu, M. Tian, G. Tao, L. Qu, Soft bimorph actuator with real-time multiplex motion perception, *Nano Energy* 76 (2020), 104926, <https://doi.org/10.1016/j.nanoen.2020.104926>.
- [43] J. Cao, Z. Zhou, Q. Song, K. Chen, G. Su, T. Zhou, Z. Zheng, C. Lu, X. Zhang, Ultrarobust $Ti_3C_2T_x$ MXene-based soft actuators via bamboo-inspired mesoscale assembly of hybrid nanostructures, *ACS Nano* 14 (2020) 7055–7065, <https://doi.org/10.1021/acsnano.0c01779>.
- [44] G. Cai, J.-H. Ciou, Y. Liu, Y. Jiang, P.S. Lee, Leaf-inspired multiresponsive MXene-based actuator for programmable smart devices, *Sci. Adv.* 5 (2019), <https://doi.org/10.1126/sciadv.aaw7956>.
- [45] M. Yang, Y. Xu, X. Zhang, H.K. Bisoyi, P. Xue, Y. Yang, X. Yang, C. Valenzuela, Y. Chen, L. Wang, W. Feng, Q. Li, Bioinspired phototropic MXene-reinforced soft tubular actuators for omnidirectional light-tracking and adaptive photovoltaics, *Adv. Funct. Mater.* 32 (2022), 2201884, <https://doi.org/10.1002/adfm.202201884>.
- [46] P. Xue, H.K. Bisoyi, Y. Chen, H. Zeng, J. Yang, X. Yang, P. Lv, X. Zhang, A. Priimagi, L. Wang, X. Xu, Q. Li, Near-infrared light-driven shape-morphing of programmable anisotropic hydrogels enabled by MXene nanosheets, *Angew. Chem. Int. Ed.* 60 (2021) 3390–3396, <https://doi.org/10.1002/ange.202014533>.
- [47] D. Zhang, J. Liu, B. Chen, Y. Zhao, J. Wang, T. Ikeda, L. Jiang, A hydrophilic/hydrophobic janus inverse-opal actuator via gradient infiltration, *ACS Nano* 12 (2018) 12149–12158, <https://doi.org/10.1021/acsnano.8b05758>.
- [48] S. Ma, Y. Zhang, Y. Liang, L. Ren, W. Tian, L. Ren, High-performance ionic-polymer–metal composite: toward large-deformation fast-response artificial muscles, *Adv. Funct. Mater.* 30 (2019), 1908508, <https://doi.org/10.1002/adfm.201908508>.
- [49] K.W. Kwan, S.J. Li, N.Y. Hau, W.D. Li, S.P. Feng, H.W.A. Ngan, Light-stimulated actuators based on nickel hydroxide-oxyhydroxide, *Sci. Robot.* 3 (2018) eaat4051, <https://doi.org/10.1126/scirobotics.aat4051>.
- [50] J. Li, L. Mou, R. Zhang, J. Sun, R. Wang, B. An, H. Cheng, K. Inoue, R. Ovalle-Robles, Z. Liu, Multi-responsive and multi-motion bimorph actuator based on super-aligned carbon nanotube sheets, *Carbon* 148 (2019) 487–495, <https://doi.org/10.1016/j.carbon.2019.04.014>.
- [51] Z. Hao, S. Song, B. Li, Q. Jia, T. Zheng, Z. Zhang, A solvent driven dual responsive actuator based on MOF/polymer composite, *Sens. Actuators B Chem.* 358 (2022), 131448, <https://doi.org/10.1016/j.snb.2022.131448>.
- [52] M. Wang, L. Zhou, W. Deng, Y. Hou, W. He, L. Yu, H. Sun, L. Ren, X. Hou, Ultrafast response and programmable locomotion of liquid/vapor/light-driven soft multifunctional actuators, *ACS Nano* 16 (2022) 2672–2681, <https://doi.org/10.1021/acsnano.1c09477>.
- [53] L. Xiong, H. Jin, Y. Lu, X. Li, X. Ai, H. Yang, L. Huang, A solvent molecule driven pure PEDOT:PSS actuator, *Macromol. Mater. Eng.* 305 (2020), 2000327, <https://doi.org/10.1002/mame.202000327>.
- [54] L. Li, J. Meng, C. Hou, Q. Zhang, Y. Li, H. Yu, H. Wang, Dual-mechanism and multimotion soft actuators based on commercial plastic film, *ACS Appl. Mater. Interfaces* 10 (2018) 15122–15128, <https://doi.org/10.1021/acsmi.8b00396>.
- [55] G. Chen, Z. Yang, W. Wang, L. Bi, L. Chen, Y. Peng, C. Ye, Electrothermal actuators with ultrafast response speed and large deformation, *Adv. Intell. Syst.* 2 (2020), 2000036, <https://doi.org/10.1002/aisy.202000036>.
- [56] G. Xu, M. Zhang, Q. Zhou, H. Chen, T. Gao, C. Li, G. Shi, A small graphene oxide sheet/polyvinylidene fluoride bilayer actuator with large and rapid responses to multiple stimuli, *Nanoscale* 9 (2017) 17465–17470, <https://doi.org/10.1039/c7nr07116g>.
- [57] J. Li, R. Zhang, L. Mou, M.J. de Andrade, X. Hu, K. Yu, J. Sun, T. Jia, Y. Dou, H. Chen, S. Fang, D. Qian, Z. Liu, Photothermal bimorph actuators with in-built cooler for light mills, frequency switches, and soft robots, *Adv. Funct. Mater.* 29 (2019), 1808995, <https://doi.org/10.1002/adfm.201808995>.
- [58] H. Li, J. Wang, Ultrafast yet controllable dual-responsive all-carbon actuators for implementing unusual mechanical movements, *ACS Appl. Mater. Interfaces* 11 (2019) 10218–10225, <https://doi.org/10.1021/acsmi.8b22099>.
- [59] Y. Hu, L. Yang, Q. Yan, Q. Ji, L. Chang, C. Zhang, J. Yan, R. Wang, L. Zhang, G. Wu, J. Sun, B. Zi, W. Chen, Y. Wu, Self-locomotive soft actuator based on asymmetric microstructural $Ti_3C_2T_x$ MXene film driven by natural sunlight fluctuation, *ACS Nano* 15 (2021) 5294–5306, <https://doi.org/10.1021/acsnano.0c10797>.
- [60] Y. Wu, J.K. Yim, J. Liang, Z. Shao, M. Qi, J. Zhong, Z. Luo, X. Yan, M. Zhang, X. Wang, R.S. Fearing, R.J. Full, L. Lin, Insect-scale fast moving and ultrarobust soft robot, *Sci. Robot.* 4 (2019) eaax1594, <https://doi.org/10.1126/scirobotics.aax1594>.
- [61] M. Duduta, F.C.J. Berlinger, R. Nagpal, D.R. Clarke, R.J. Wood, F.Z. Temel, Electrically-latched compliant jumping mechanism based on a dielectric elastomer actuator, *Smart Mater. Struct.* 28 (2019) 09LT01, <https://doi.org/10.1088/1361-665X/ab3537>.
- [62] X. Huang, K. Kumar, M.K. Jamed, A.M. Nasab, Z. Ye, W. Shan, C. Majidi, Chasing biomimetic locomotion speeds: creating untethered soft robots with shape memory alloy actuators, *Sci. Robot.* 3 (2018) eaau7557, <https://doi.org/10.1126/scirobotics.aau7557>.
- [63] C. Ahn, X. Liang, S. Cai, Bioinspired design of light-powered crawling, squeezing, and jumping untethered soft robot, *Adv. Mater. Technol.* 4 (2019), 1900185, <https://doi.org/10.1002/admt.201900185>.